PRAMANA
— journal of
physics

Vol. 59, No. 1
July 2002
pp. 33–51

Effects of non-local thermodynamic equilibrium conditions on numerical simulations of inertial confinement fusion plasmas

N K GUPTA* and B K GODWAL
High Pressure Physics Division, Bhabha Atomic Research Centre, Mumbai 400 085, India
*Email: nkgupta@apsara.barc.ernet.in

MS received 27 September 2001; revised 31 January 2002

Abstract. Effects of non-local thermodynamic equilibrium (non-LTE) condition on emission and hydrodynamics of typical inertial confinement fusion (ICF) plasmas are studied. The average degree of ionization at high temperatures is seen to be much lower compared to the values obtained from Thomas–Fermi scaling or Saha equation for high-Z element like gold. LTE and non-LTE predictions for emitted radiation from laser-driven gold foil are compared with the experimental results and it is seen that non-LTE simulations show a marked improvement over LTE results. The effects of one group and multigroup, LTE and non-LTE approximations of radiation transport on hydrodynamic parameters are studied for laser-driven aluminium and gold foils. It is further seen that non-LTE and multigroup effects play an important role in predicting conversion efficiency of laser light to X-rays.

Keywords. Non-LTE; opacity; emissivity; ICF; radiation transport; hydrodynamics; conversion efficiency.

PACS Nos 28.52.av; 28.52.cx; 52.55.Pi; 52.70.Nc

1. Introduction

Most of the present day inertial confinement fusion (ICF) experiments are based on the concept of indirect-drive [1]. Although some of the smoothing devices like random phase plate (RPP), smoothing by spectral dispersion (SSD), induced spatial incoherence (ISI) etc. [2] have kept alive the interest in direct drive experiments, indirect-drive fusion schemes have a distinctive advantage because of uniform radiation inside the cavity or hohlraum. The uniformity of the radiation inside the hohlraum is of great significance for the success of ICF experiments. For example, it is shown by Ermolovich *et al* [3] that a non-uniformity of 5% in the radiation temperature on pellet surface can reduce the neutron yield by a factor of seven. The current high pressure experiments are essentially using the hohlraum as a source of soft X-rays to drive the shock wave in the material. To minimize the energy loss in converting laser or ion beam to X-rays, high absorption and re-emission from hohlraum walls is required. This requires the use of high-Z material and gold has been the most widely used material so far for the ICF hohlraums. Recently, it has been proposed to use a mixture of two or more high-Z elements [4] for hohlraum walls. These studies have shown

that it is possible to obtain higher Rosseland mean opacity as compared to either of the elements in the mixtures. This in turn can lead to higher conversion efficiency of laser light and hence higher radiation temperatures. To numerically simulate an indirect-drive ICF experiment, the two basic requirements are the computations of the frequency dependent radiation opacities and radiation hydrodynamics. Any prescription to calculate opacities must include bound-bound transitions as its absence can change the results by a factor of two. A simple screened hydrogenic atom model is widely used to calculate atomic properties [5]. In this model, the electronic states are characterized only by the principal quantum number n. Tsakiris and Eidmann [6] introduced an artificial linewidth with each line to reproduce reasonably well the Rosseland and Planck means using this simple model. For the case of Eu ($Z = 63$), they proposed a uniform width of 100 eV to all lines which reproduces well the material opacity means for a wide density and temperature range. Takabe *et al* [7] showed that a uniform width of 150 eV predicts well the X-ray conversion efficiency for intense laser light from gold. However, the choice of the linewidth remains arbitrary. Rickert and Meyer-ter-Vehn [8] introduced the ℓ splitting in this model and as a result removed the need for artificial line broadening. The need of non-LTE model to calculate the opacity and emissivity is well established [9]. Whitney *et al* [10] had shown that to enforce LTE conditions for highly ionized aluminium, a density of 45 g/cm^3 is required. Kiyokawa *et al* [11] had demonstrated the need of non-LTE coefficients to reproduce the experimentally observed emitted spectrum from laser irradiated gold foil. On hydrodynamic time scales, the ICF plasmas have strong time and space gradients and hence there is not enough time for equilibrium to be established. Even in the case of homogeneous and time independent plasma, non-LTE conditions exist if plasma is of finite size and photon can escape it [12]. In §2 of this paper, we describe the non-LTE model adopted for computing the absorption and emission coefficients. The steady state conditions are assumed for ionic population. Taking gold as a representative material, we also compare our results for the frequency dependent opacities and emissivity with other models.

The radiation generation and transport plays a significant role in the direct [13] as well as indirect-drive inertial confinement fusion schemes. The numerical simulations of the indirect-drive ICF experiments involve the conversion of the incident beam energy into X-rays, its redistribution in the hohlraum by multiple absorptions and re-emissions, and finally the radiation-driven hydrodynamics of the fusion capsule inside the hohlraum. The radiation transport plays a crucial role in all the above three processes. It is also well known that the radiation can pre-heat the target and reduce the overall compression [14]. Marchand *et al* [15] have shown that for aluminium, the radiation transport increases the ablated mass significantly. The coupled radiation hydrodynamics can be modeled either in one group gray approximation [16] or using sophisticated computer codes based on multigroup models [17]. We briefly describe our model for the radiation transport in §3 of the paper. To test the models of hydrodynamics, opacity and emissivity, we simulate two experiments. The first experiment considered is that of Nishikawa *et al* [18] where the emitted intensity spectrum from the front side of a laser-driven thin gold foil is measured. Secondly, we analyze the experiment of Kauffman *et al* [19] where an aluminium wedge is driven by radiation from hohlraum. The main results of these studies are presented in this section. In §4 of the paper, we demonstrate the importance of multigroup transport of radiation for laser-driven aluminium and gold foils. It is also shown that non-LTE and multigroup effects play important roles in predicting the conversion efficiency of laser light into X-rays. Finally, we conclude the article in §5.

2. Absorption and emission coefficients

2.1 *Energy levels*

The exact solutions of Schrödinger or Dirac equation are known for hydrogen atom only. Even for helium, the problem of calculating the accurate wave functions and energy levels is very difficult. The computational complexity increases rapidly as we go to many electron systems. The present day accurate methods are based on self-consistent Hartree–Fock (HF) models [20]. However, these calculations are computationally expensive and one resort to approximate models. We adopt one such model which is used extensively. The energy levels of partially ionized ions are calculated using the screened hydrogenic model including the ℓ splitting. The 10×10 matrix of the screening constants used is the one proposed by More [5]. The ℓ splitting introduces additional 20 constants as given by Perrot [21]. We may, however, mention here that the ℓ splitting in our model is incorporated as a correction to ℓ degenerate energy levels. Recently, Faussurier *et al* [22] have introduced the screening coefficients including the ℓ splitting and the use of these coefficients may be a better choice. jj Coupling and relativistic corrections are neglected. These corrections lead to further splitting of the energy levels and screening coefficients, which are obtained from an elaborate fitting of available data on energy levels, and are not available with these splitting. In the adopted atomic model, the one electron energies are given by (in atomic units)

$$E_{n\ell} = E_n - \sum_m P_m(q_{nm}S_m - q_{mn}Sn) - \frac{Z_n}{n^2} g_{n\ell} \sum_m P_m q_{mn} \tag{2.1}$$

with

$$S_n = \frac{Z_n}{n^2} \sum_{\ell=0}^{n-1} \frac{P_{n\ell}}{Pn} g_{n\ell} \tag{2.2}$$

and the screened nuclear charge Z_n is given by

$$Z_n = Z - \sum_{m \le n} P_m \sigma_{nm}(1 - 0.5\delta_{nm}) + \sum_m P_m q_{mn} \sum_{\ell=0}^{n-1} \frac{P_{n\ell}}{P_n} g_{n\ell.} \tag{2.3}$$

Here Z denotes the nuclear charge of the material, σ the screening constant matrix as proposed by More [5], $P_{n\ell}$ the occupation number of the atomic sub-shell (n, ℓ) and $P_n = \sum_l P_{n\ell}$ gives the occupation number of shell n. $P_{n\ell}$ used in our model are as obtained from degeneracy of each level in the respective ion. Ions are assumed to be in the ground state. The parameter $g_{n\ell} = 0.25[n^2 - 2\ell(\ell+1) - 1]/n^2 + \nu_n^2$ and the constants ν_n and q_{nn} are taken from Perrot [21]. The ℓ degenerate one electron energies E_n are given by

$$E_n = -\frac{Z_n^2}{2n^2} + \sum_{m \ge n} Pm\sigma_{nm}(1 - 0.5\delta_{nm}) \frac{Z_m}{m^2}. \tag{2.4}$$

This model is being widely used because of its simplicity when compared to more elaborate HFS calculations. It reproduces the energy levels for neutral as well as ionized atoms to reasonable accuracy [8]. As an example, in figure 1 we show the ionization potential

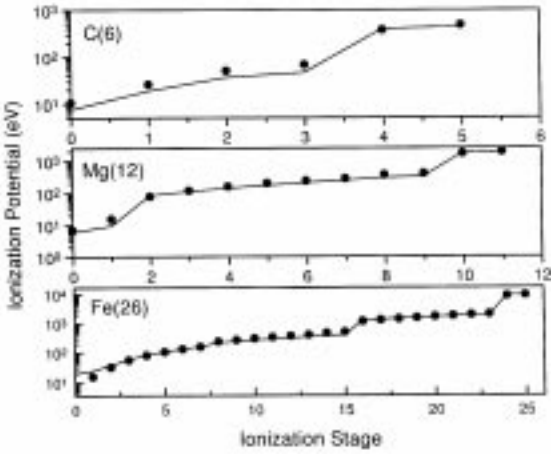

Figure 1. Ionization potential for three representative elements. The solid line represent the calculated values while filled circles give experimental data. The degree of ionization is varied from 0 (neutral atom) to Z-1.

as a function of state of ionization for three representative elements. The solid lines in this figure give the ionization potential as calculated by the above model while the solid circles are the experimental values as tabulated by Carlson *et al* [23]. It is seen from this figure that a good agreement exists between calculated and experimental values.

2.2 *Population densities of ions*

The population densities of neutral to fully ionized ions for any element in the mixture are obtained by solving the steady-state rate equations. Steady-state conditions for rate equations can be assumed as long as collision time for ionization is short which is often the case in laser produced plasmas [24]. The atomic processes considered are the collisional ionization, three body recombination, radiative recombination, and di-electronic recombination. The process of photo ionization is not included in the rate equation as it is usually small compared to collissional ionization for ICF plasmas. As a rough order of estimate, we note that the ratio of ionization rate of unexcited atoms by electron impact and by photons (assuming the radiation to be in equilibrium with matter) can be approximated as $1.710^{-16} n_e/(IT^{1/2})$ [25]. The ionization potential I and the temperature T are in electron volts. This implies that for $T \sim 100$ eV, $I \sim 10$ eV, the electron density should be $\geq 10^{18}$ which is true for the most part of the ICF plasmas. In the following we use the subscript s to denote the state of ionization. For neutral atom s is 0 while it is equal to atomic number Z for a fully ionized ion. The number density of s-fold ionized ion n_s is given by the rate equation (steady-state)

$$n_{s+1} n_e^2 \beta_{s+1} + n_{s+1} n_e \alpha_{s+1} + n_{s+1} n_e D_{s+1} - n_s n_e C_s = 0 \tag{2.5}$$

where β_{s+1}, α_{s+1} and D_{s+1} are the coefficients for collisional, radiative and di-electronic recombination respectively. C_s denotes the electronic collisional ionization coefficient. The

electron density is denoted by n_e and the ion density for the element under consideration in the mixture is $n_i = \sum n_s$.

Coefficients for collisional and radiative recombination as well as the electronic collisional ionization are taken from Eidmann [9]. Di-electronic recombination becomes important at high temperatures and low densities. We use the formulation of Post *et al* [26] which is a modification of the formula originally proposed by Burgess [27]. The details of the formulae used for di-electronic recombination coefficient can be found in MacFarlane [28] who uses the same formulation in the code IONMIX. The steady state solution of eq. (2.5) gives the ion densities as

$$\frac{n_{s+1}}{n_s} = \frac{C_s}{n_e\beta_{s+1} + \alpha_{s+1} + D_{s+1}}. \tag{2.6}$$

The Saha equation and the corona equilibrium are the two limiting cases of the above equation for large and small electron density n_e. The above equation together with the consistency condition $\sum_s n_s = n_i$ is solved to obtain all n_s and the average degree of ionization.

In figure 2 we show the calculated average degree of ionization for gold. The density considered is 0.1 g/cm^3 and temperature is varied from 10 eV to 10 keV. The present model results are marked as NLTE and also shown are the values obtained from Thomas–Fermi scaling law (TF) [29] and the solution of the Saha equation (SAHA). We note that results from Thomas–Fermi agree with the solution of Saha equation (except for shell effects). We further note that at low temperatures (up to 100 eV), simple models like TF and SAHA estimates of the average degree of ionization are close to non-LTE results. However, at higher temperatures these simple models overpredict the ionization. The lower values of ionization by non-LTE model is in conformity with the earlier results of Eidmann [9]. Knowing the population of the ions, the level population $n_{n\ell}(s)$ is obtained through standard Boltzmann relation [30] with level energies as calculated in §2.1. The Boltzmann equation is solved together with the consistency condition $\sum_{n\ell} n_{n\ell}(s) = n_s$.

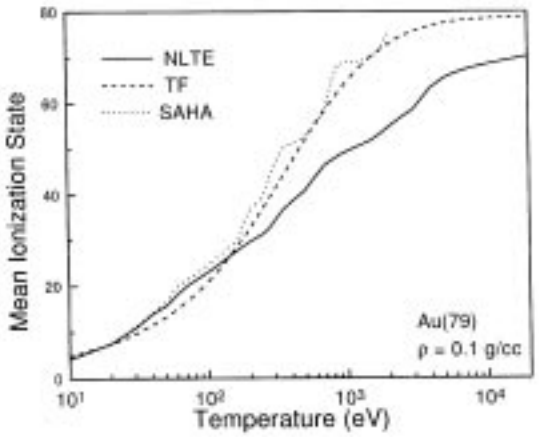

Figure 2. The average degree of ionization as a function of temperature for gold at a density of 0.1 g/cm^3. The solid line gives the non-LTE results while dashed and dotted lines respectively correspond to Thomas–Fermi scaling law and solution of Saha equation.

2.3 *Opacities and emissivity*

Absorption and emission coefficients at a photon frequency ν for any element in the mixture are given by

$$\kappa(\nu) = \frac{1}{\rho}\left[\sum_{s=0}^{Z}\{\kappa_{\rm bb}(s,\nu)+\kappa_{\rm bf}(s,\nu)+\kappa_{\rm ff}(s,\nu)\}\right]+S^{\rm T}(\nu)+S^{\rm P}(\nu), \tag{2.7}$$

$$\varepsilon(\nu) = \frac{2h\nu^3}{c^2}\sum_{s=0}^{Z}\{\varepsilon_{\rm bb}(s,\nu)+\varepsilon_{\rm bf}(s,\nu)+\varepsilon_{\rm ff}(s,\nu)\}, \tag{2.8}$$

where ρ denotes the density of the plasma. The suffices bb, bf and ff respectively represent the contribution of bound–bound, bound–free and free–free transitions to absorption and emission coefficients. $S^{\rm T}(\nu)$ and $S^{\rm P}(\nu)$ respectively denote the contribution of Thomson scattering and plasma oscillations to absorption coefficient. Here, κ is in units of $\rm cm^2/g$ and the emission coefficient is in $\rm ergs/cm^3/sterad$. In general, emission and absorption coefficients depend on density, temperature and also on radiation intensity because of photo-ionization and photo-excitation processes. These effects are neglected here and as a result we have only two-dimensional tables for these coefficients in the hydrodynamic simulations presented in §§3 and 4. This limits the applicability of the model to the situations where radiation intensities are not very high. Knowing the frequency dependent coefficients, the Rosseland and Planck means are obtained using standard weighting functions [30].

The bound–bound contributions to absorption and emission are given by

$$\kappa_{{\rm bb}(\nu,s)} = \frac{\pi e^2}{mc}\sum_{n\ell}\sum_{n'\ell'}\left[1-\frac{g_{n\ell}n_{n'\ell'}(s)}{g_{n'\ell'}n_{n\ell}(s)}\right]n_{n\ell}(s)\,f_{n\ell,n'\ell'}(\nu,s)\Psi_{n\ell,n'\ell'}, \tag{2.9}$$

and

$$\varepsilon_{{\rm bb}(\nu,s)} = \frac{\pi e^2}{mc}\sum_{n\ell}\sum_{n'\ell'}\left[\frac{g_{n\ell}n_{n'\ell'}(s)}{g_{n'\ell'}n_{n\ell}(s)}\right]n_{n\ell}(s)\,f_{n\ell,n'\ell'}(\nu,s)\Psi_{n\ell,n'\ell'}, \tag{2.10}$$

where $\Psi_{n\ell,n'\ell'}$ denotes the line profile for which we use the Lorentzian shape. Standard formulae are used for natural, stark and Doppler widths. The fine structure broadening is calculated in a hydrogenic approximation [31] and the electron collisional broadening is calculated as given by Armstrong [32]. The detailed expressions of these broadenings are given by Rickert and Meyer-ter-Vehn [8]. The oscillator strength $f_{n\ell,n'\ell'}(\nu,s)$ for transition from state $n\ell$ to $n'\ell'$ is given by

$$f_{n\ell,n'\ell'}(\nu,s) = \frac{1}{3}\frac{\max(\ell,\ell')}{2\ell+1}\frac{\Delta E}{13.6}\left(R_{n\ell}^{n'\ell'}\right)^2 P_{n\ell}\left(1-\frac{P_{n'\ell'}}{2(2\ell'+1)}\right), \tag{2.11}$$

where $P_{n\ell}$ denotes the number of electrons in the bound level $n\ell$. The radial integral $R_{n\ell}^{n'\ell'}$ are evaluated as per the prescription of Naqvi [33].

The bound–free contributions are given by

$$\kappa_{\mathrm{bf}(\nu,s)} = \sum_{n\ell}\left[1 - \frac{n^*_{n\ell}(s)}{n_{n\ell}(s)}\exp\left(-\frac{h\nu}{kT}\right)\right] n_{n\ell}(s)\, f_{n\ell,f}, \tag{2.12}$$

$$\varepsilon_{\mathrm{bf}(\nu,s)} = \sum_{n\ell}\exp\left(-\frac{h\nu}{kT}\right) n^*_{n\ell}(s)\, f_{n\ell,f}, \tag{2.13}$$

where $n^*_{n\ell}$ denotes the LTE population [30] of the state $n\ell$ and

$$f_{n\ell,f} = h\nu\sqrt{\lambda}P_{n\ell}\left(1 - \frac{1}{1+\mathrm{e}^{\lambda/T}}\right)\left[\frac{\ell+1}{2\ell+1}\left(R^{\lambda,\ell+1}_{n\ell}\right)^2 + \frac{\ell}{2\ell+1}\left(R^{\lambda,\ell-1}_{n\ell}\right)^2\right]. \tag{2.14}$$

The radial integrals are again evaluated as given by Naqvi [33] and $\lambda = h\nu - \left|E_{n\ell}\right|$. The free–free (inverse bremsstrahlung) contributions to absorption and emission are given by

$$\kappa_{\mathrm{ff}(\nu,s)} = n_e n_s(1 - \mathrm{e}^{-h\nu/kT})\sigma^{\mathrm{ff}}(s), \tag{2.15}$$

$$\varepsilon_{\mathrm{ff}(\nu,s)} = n_e n_s \mathrm{e}^{-h\nu/kT}\sigma^{\mathrm{ff}}(s), \tag{2.16}$$

with the free–free cross-section as

$$\sigma^{\mathrm{ff}}(s) = \frac{4}{3}\sqrt{\left(\frac{2\pi}{3mk_{\mathrm{B}}T}\right)}\frac{s^2e^6}{hmc\nu^3}g_{\mathrm{ff}}. \tag{2.17}$$

The various symbols have their usual meaning and the free-free gaunt factor $g_{\mathrm{ff}} = 1 + 0.44\exp([-0.25(\gamma^2+0.25)^2]$ and $\gamma^2 = \log_{10}\left(13.6\frac{\langle Z^2\rangle}{T}\right)$. The average square charge $\langle Z^2\rangle = \sum_s s^2 n_s/n_i$. The Thomson scattering term is given by

$$S^T(\nu) = \frac{8\pi e^4}{3m^2c^4}[n_e + n_e^B(\nu)], \tag{2.18}$$

where $n_e^{\mathrm{B}}(\nu)$ denotes the contribution of bound electrons which act as free electrons when the photon energy is greater than the binding energy of the bound electrons. The plasma oscillation term $S^{\mathrm{P}}(\nu) = [\omega_{\mathrm{p}}^2 - (2\pi\nu)^2]^{1/2}/c$ where ω_{p} is the plasma frequency. This term is present only when the photon energy is less than the energy corresponding to plasma frequency.

For the case of mixtures, the bound–bound and bound–free contributions to opacities are obtained as weighted average. The weights for each element in the mixture are taken as the respective number fraction. Free–free contribution to opacities of mixture is obtained using weighted average ionization of the mixture. The average degree of ionization of the mixture is obtained from the individual element ionization with their fraction density as the weights [34].

As an example we plot in figures 3 and 4 the frequency dependent absorption and emission coefficients respectively for gold as calculated by the above model at a temperature of 500 eV and a density of 0.1 g/cm^3. We have chosen these values of density and temperature so that we can compare our results with the ℓ degenerate values from the model of Eidmann [9]. The free–free and bound–free contributions are also shown separately in these figures. Comparing this with figure 3 of Eidmann [9] we observe a qualitative agreement between the two models. In figure 3 we have also shown by dotted line the absorption coefficient as calculated by the code IONMIX [28]. We note that bound-free contribution

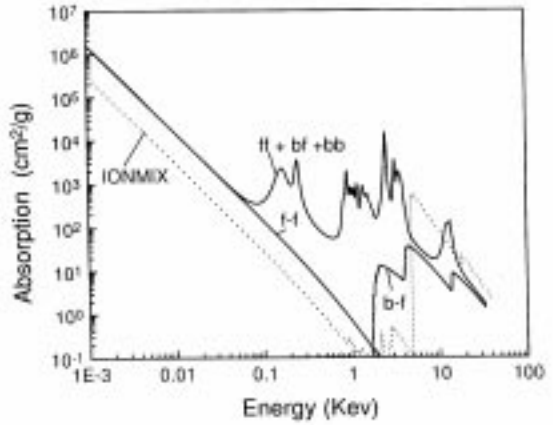

Figure 3. Calculated absorption coefficient as a function of photon energy for gold at a temperature of 500 eV and a density of 0.1 g/cm^3. The dotted line gives the results from the code IONMIX. The curves marked b–f and f–f represent the bound–free and free–free contribution respectively.

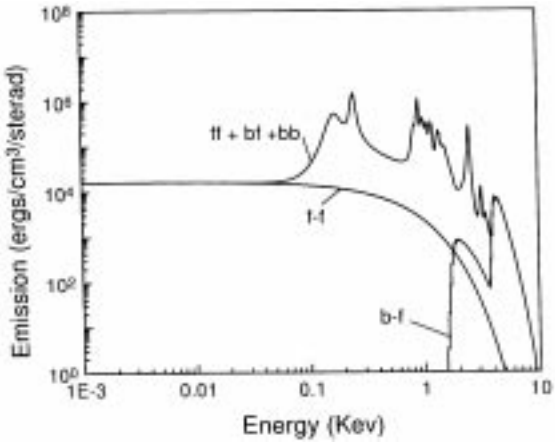

Figure 4. Calculated emission coefficient as a function of photon energy for gold at a temperature of 500 eV and a density of 0.1 g/cm^3. The curves marked b–f and f–f represent the bound–free and free–free contributions respectively.

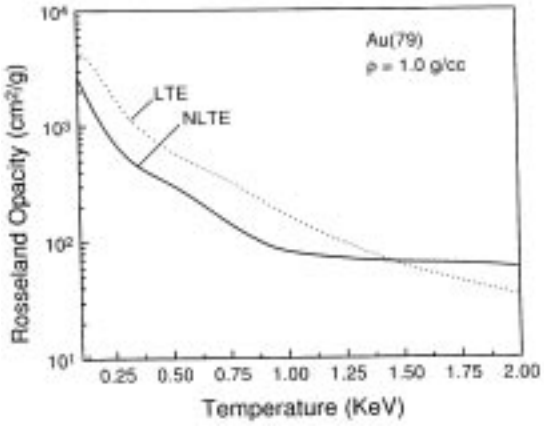

Figure 5. Rosseland mean opacity as a function of temperature for gold at a density of 1.0 g/cm^3. The solid and dashed lines respectively give the results for non-LTE and LTE cases.

is significant only for photon energies above 1.7 keV and line contribution is important for frequencies beyond 200 eV. At lower energies, it is basically the inverse bremsstrahlung which dominates the absorption coefficient and becomes small beyond 2 keV. As an example of Rosseland mean opacity, we show in figure 5 the calculated value of it for gold as a function of temperature for a density of 1.0 g/cm^3. The dotted line in this figure show the Rosseland mean as calculated by similar average atom model [35] in the LTE conditions. The temperature is varied from 100 eV to 2 keV. We note that up to about 1.3 keV, the average atom LTE model overpredicts the opacity as compared to non-LTE model and beyond that the trend changes. At high temperatures we have already seen that LTE models overpredicts the degree of ionization (figure 2). As a result, the bound-bound and bound-free contributions to opacities are underpredicted by these models and this leads to lower values for Rosseland mean at higher temperatures by LTE models.

3. Hydrodynamic simulations

The hydrodynamics is treated by solving the three standard conservation (mass, momentum and internal energy) equations in one-dimensional Lagrangian geometry [25]. The shocks are treated by Von-Neumann artificial viscous pressure procedure [36]. The material pressure is related to the density and internal energy through a tabulated equation of state (EOS). The laser energy deposition is calculated via inverse bremsstrahlung up to the critical density and a pre-specified fraction of the remaining power is dumped at this density. Most of the thermal flux is carried by the electrons and is calculated using the flux limited Spitzer's formula [37]. Radiation transport is treated by either multigroup radiation diffusion approximation or by discrete direction Sn method [16]. Tabulated opacity and emissivity data are used and they are generated by the model described in §2. The basic equations and the other details of the radiation hydrodynamic programme are given by Gupta and Kumar [38] and are therefore not repeated here. In the following two sub-

sections we present our hydrodynamic simulation results for gold and aluminium foils. A comparison is made between the LTE and non-LTE model predictions. Comparisons with experimental results clearly establish the need of non-LTE coefficients for both these materials.

3.1 *Laser-driven gold foil*

To bring out the importance of non-LTE effects for gold, we choose the experiment of Nishikawa *et al* [18]. In this experiment a gold foil of 0.436 μm thickness was irradiated by six laser beams with wavelength of 0.35 μm and a spot radius of 0.5 mm. The laser has an intensity of 3.3×10^{14} W/cm^2 and pulse duration of 800 ps. The spectrum of the emitted radiation from the front side of the target was measured in this experiment. The experimentally measured spectrum taken from the above paper is shown in figure 6 by dashed–dotted line. Similar structure in the spectra was also measured in OMEGA experiments on gold-coated spheres [39]. It shows a strong peak at about 200 eV. We have simulated this experiment with the multigroup radiation transport model described above using the diffusion approximation. We used 75 frequency groups equally spaced in lethargy variable. The use of lethargy variables gives higher number of groups for lower energies. The opacity and emissivity tables were generated for the gold using the model described in §2. In these tables, 21 temperature points are used to cover temperatures up to 5 keV while nine density points are used for a density range from 1.0×10^{-6} times the solid density to 100 times the solid density. We have used a coarse mesh grid for opacity tables, specifically for density. This is guided by the low values of the exponent in the Rosseland and Planck means scaling with density [6] (0.481 and 0.483 for aluminium, 0.001 and

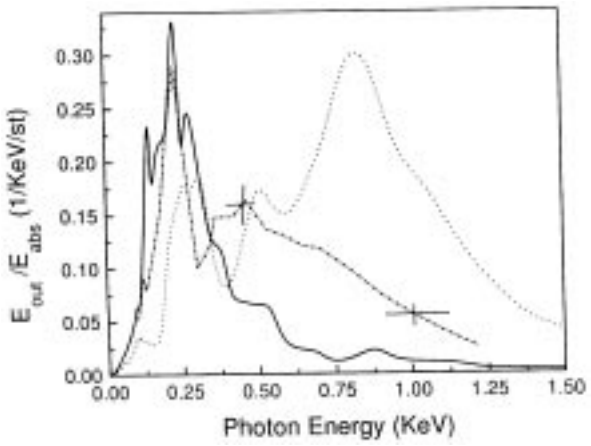

Figure 6. Time integrated normalized spectra of radiations emitted from a 0.436 μm-thick gold foil driven by 0.35 μm wavelength, 800 ps (FWHM) laser pulse. Dashed–dotted line gives experimental values of Nishikawa *et al*, while solid and dashed curves respectively represent our numerical simulation results in the non-LTE and LTE conditions.

0.165 for gold). For temperature, we have used a non-uniform mesh with finer points in the intermediate range of temperatures. Ideal gas equation of state (EOS) is used for ions. This may introduce some errors at high densities. The electron EOS data is generated by subtracting the ion contribution from SESAME [40] tables. The spectrum of the emitted radiation from the front side of the foil is shown by solid line in figure 6. We observe that the peak at 200 eV is well reproduced. Also shown in this figure by dotted line is the emitted spectrum when we use an average atom LTE model to calculate the opacities and use Kirchoff's law to obtain the emission. We observe that LTE results show a much stronger peak at about 800 eV which is not observed in the experiment. It is interesting to note that our LTE spectrum qualitatively agrees with the LTE simulations using the code ILESTA of Nishikawa *et al* [18]. They have also shown in their paper that the calculated spectra can be made to agree better with experiment if new modified coefficients for absorption and emission are used in the radiation transport. This comparison clearly brings out the importance of non-LTE coefficients to explain the emitted spectrum from laser-driven thin gold foils. Although the differences between measured and calculated spectrum for photon energies greater than 300 eV is large even for non-LTE case, the improvements over the LTE case is clearly visible up to 300 eV and beyond 600 eV. However, relatively small peak at about 500 eV observed in the experiment is not reproduced by the present non-LTE model.

3.2 *Radiation-driven aluminium foil*

As a test for low Z material, we have simulated the experiment of Kauffman *et al* [19]. A wedge-shaped aluminium foil was driven by hohlraum radiation in NOVA experiments. The temperature of the radiation in the cavity was estimated in two different ways. Using the scaling laws of shock speed vs. radiation temperature for aluminium, Kauffman *et al* estimated a radiation temperature of 207 eV. On the other hand, re-emission from the X-ray heated wall is used to estimate time dependent radiation brightness temperature. It gives an initial temperature of about 135 eV and reaches a peak of 200 eV in about 2.1 ns. We have simulated this experiment using the hydrodynamic model described above. Non-LTE opacity and emissivity tables were generated in 75 frequency groups. For the purpose of comparisons, we have also analyzed this experiment using LTE model. EOS tables used were obtained as described in §3.1. Results of our numerical simulation for the incident hohlraum radiation temperature of 207 eV are shown in figure 7. The solid curve in this figure gives the penetration depth of radiation-driven shock as obtained from the non-LTE model. The corresponding results using the LTE coefficients are shown by dotted line. The solid circles give the experimental results taken from the paper of Kauffman *et al* [19]. We note that for earlier times (up to 2.3 ns) both LTE and non-LTE models give higher penetration depth as compared to experimental results. This may be attributed to the lower incident radiation temperatures compared to 207 eV in the experiment. At later times, the non-LTE results agree well with the experimental points while LTE model shows a much faster penetration of shock front. A linear fit to the data gives a shock speed of 4.72 cm/μs for non-LTE model as compared to 5.06 cm/μs for LTE model. The reported experimental speed is 4.88 cm/μs. This clearly establishes the need of non-LTE coefficients for analyzing the radiation-driven hydrodynamics in aluminium foils.

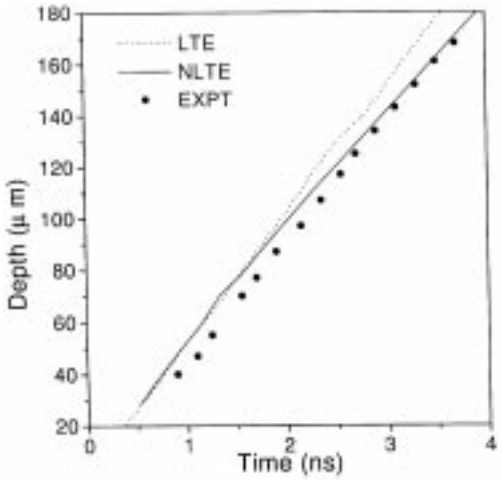

Figure 7. Penetration depth of 207 eV radiation-driven shock wave in aluminium foil. Filled circles are the experimental values of Kauffman *et al* while solid and dashed curves respectively represent our numerical simulation results for the non-LTE and LTE conditions.

4. Radiation transport effects

In this section we study the effects of radiation transport on hydrodynamic parameters of typical ICF plasmas. We study the differences in one group and multigroup predictions. We also study the effects of non-LTE plasma conditions. For these studies, we consider the planer foils driven by a 200 ps (FWHM) Gaussian Nd glass laser of peak intensity of 5×10^{13} W/cm^2. As representative of low and high Z targets, the two elements considered in this study are aluminium and gold. These are extensively studied elements because of their well-tested equation of state data. The laser beam absorption is assumed to be via inverse bremsstrahlung up to the critical density and remaining energy is dumped in few numerical space meshes near the critical density. Although for the laser parameters considered, typically 40 to 60% of laser light is expected to be scattered back [41], we have assumed a 100% absorption of the beam to avoid any uncertainties associated with anomalous absorption mechanisms. Thus, the laser intensity in our simulations refers to the absorbed energy rather than the incident energy. The hydrodynamics is modelled with the 1-D, two-temperature (electron and ion), multigroup Lagrangian geometry code as described in §3. The electron and ion EOS tables used are obtained as described in §3.1. The free streaming flux limiting parameter f is taken to be 0.03 for all the studies presented here. It is well known that the free streaming parameter can change the results of numerical simulations [42]. This parameter is not known exactly and one tries to adjust it so as to get best possible comparison with the experiments. As our aim in this section is not to reproduce experimental results but to study the effects of various models on hydrodynamic parameters, we have fixed a representative value of 0.03 for it. The radiation transport is modelled in one and multigroup diffusion approximation. The multigroup Planck and Rosseland mean opacities as well as the emissivities are interpolated from the tables generated using the model described in §2.

In figure 8 we show the time profiles of the maximum electron, ion and radiation temperatures for a 6 μm-thick aluminium foil driven by the above described laser beam with a peak power of 5×10^{13} W/cm^2. In this as well as in all the other subsequent figures, the solid, dashed and the dotted curves respectively denote the cases of no radiation transport (NRT), one group of radiation transport (1GNRT) and the 75 groups of radiation transport (75GRT). The ion and electron temperatures are observed to be nearly the same in cases of 75GRT and 1GRT and therefore 1GRT results are not presented for them. However, they are lower as compared to the case of no radiation temperature. For example, the peak electron temperatures in the corona region of plasma are 2.13 keV and 388 eV respectively in the cases of NRT and 75 GRT. This is essentially due to radiation cooling of hot corona region. Further, we observe that in the corona region the ion temperatures are lower than the electron temperatures and they are higher than the radiation temperatures. It indicates that the electrons, ions and the radiation are not in thermodynamic equilibrium and the plasma is in a non-LTE state. This is in conformity with the earlier studies of Whitney *et al* [10] where it is shown that for highly ionized aluminium plasma, the LTE conditions require very high densities ($\sim$45 g/cm^3). To see the importance of non-LTE conditions, we have repeated the above simulations for LTE conditions. The radiation opacities were calculated using an average atom model and Kirchoff's law is used to calculate the emissivity. These results are presented in figure 9.

In figure 10 we show the time profiles of ablated mass and the maximum density for the above three cases. The solid, dashed and the dotted curves respectively denote the cases of no radiation transport (NRT), one group of radiation transport (1GRT) and the 75 groups of radiation transport (75GRT). We note that multigroup radiation transport leads to much higher mass ablation as compared to the one group and no radiation transport cases. This result is consistent with the mass ablation rate reported earlier by Marchand *et al* [15] for nano second laser pulse. The larger mass ablation essentially arises because of more heat conduction from critical density position to the ablation front due to the radiation transport. We further note that the gray approximation results do increase the mass ablation rate as compared to the NRT case but the increase is much more significant

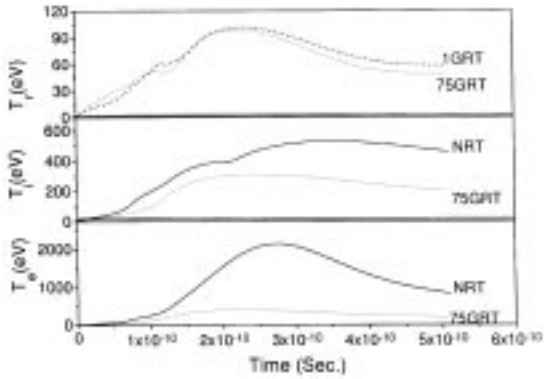

Figure 8. Non-LTE simulation results for maximum electron, ion and radiation temperatures as a function of time for aluminium foil driven by 200 ps laser beam. Solid, dashed and dotted curves respectively show results for the cases of no, one group and 75 groups of radiation transport.

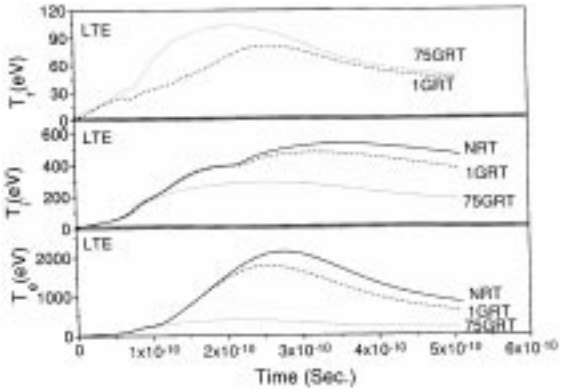

Figure 9. LTE simulation results for maximum electron, ion and radiation temperatures as a function of time for aluminium foil driven by 200 ps laser beam. Solid, dashed and dotted curves respectively show results for the cases of no, one group and 75 groups of radiation transport.

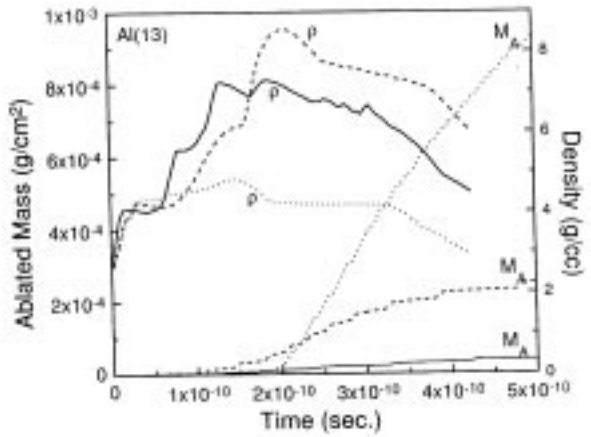

Figure 10. Ablated mass and maximum density as a function of time for aluminium foil driven by 200 ps laser beam. Solid, dashed and dotted curves respectively show results for the cases of no, one group and 75 groups of radiation transport.

in the case of multigroup radiation transport simulations. In figure 11 we show the space profiles of density and pressure at 200 ps. We note that 75GRT predicts much higher ablation pressure (15.4 Mbar) as compared to the case of 1GRT (7.0 Mbar) and NRT (6.6 Mbar). This is essentially because of higher mass ablation rate in case of multigroup simulations as compared to the other two cases. The maximum density behind the shock front is observed to be lower (4.67 g/cm^3) as compared to the 1GRT (7.0 g/cm^3) and the NRT (6.8 g/cm^3) cases. This is because of preheating of the foil leading to lower compression. We also note that the rarefaction wave has already started moving from the rare side of the foil in the case when radiation transport is included.

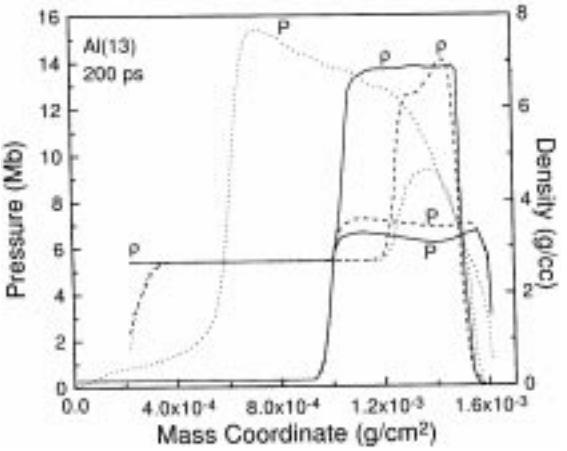

Figure 11. Non-LTE simulation results for space profiles for density and pressure at 200 ps for aluminium foil driven by 200 ps laser beam. Solid, dashed and dotted curves respectively show results for the cases of no, one group and 75 groups of radiation transport.

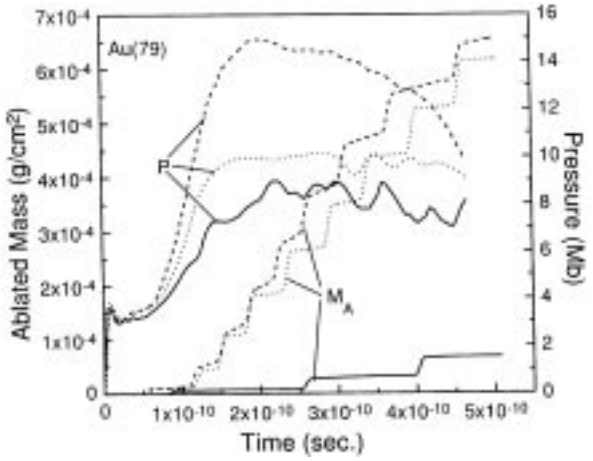

Figure 12. Ablated mass and maximum pressure as a function of time for gold foil driven by 200 ps laser beam. Solid, dashed and dotted curves respectively show results for the cases of no, one group and 75 groups of radiation transport.

In figure 12 we show the time profiles of the ablated mass and the maximum pressure for the 6 μm-thick gold foil. Here again we observe the importance of radiation transport. However, here we note that one group grey approximation gives higher mass ablation as compared to multigroup simulations. This implies that in case of high Z element like gold, the grey approximation is not sufficient and one should go for multigroup radiation transport. We know that for aluminium as well as gold the plasma is optically thin for high energy photons and it is optically thick for low energy photons. A multigroup approach

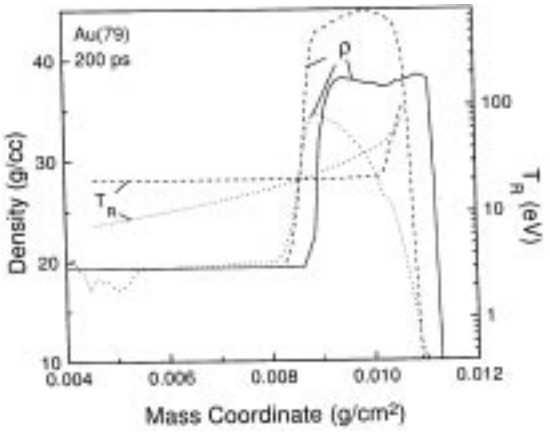

Figure 13. Computed space profiles for density and radiation temperature at 200 ps for gold foil driven by 200 ps laser beam. Solid, dashed and dotted curves respectively show results for the cases of no, one group and 75 groups of radiation transport.

takes into account these effects while one group approach relies on a mean over the entire photon energy range. The aluminium plasma seems to be optically thick for this one group mean and hence an underprediction of radiation transport. On the other hand, the gold plasma appears to be optically thin for the one group mean and hence in this case one group approximation overpredicts the radiation effects as compared to multigroup radiation transport. One group transport predicts the maximum ablation pressure of 14.9 Mbar as compared to 10.2 Mbar in case of 75 frequency groups. If we ignore the radiation transport, a much lower ablation pressure of 9.0 Mbar is obtained. This is essentially a consequence of different mass ablation rates as in the case of aluminium. In figure 13 we show the space profiles of density and radiation temperatures at 200 ps. From this figure we note that multigroup and one group models predict almost the same shock speed, although the compression is higher in the case of multigroups. The radiation temperature profile is much more uniform in case of multigroup case as compared to the one group approximation.

In figure 14 we show the conversion efficiency of laser light to X-rays (ratio of total energy radiated on the side of laser irradiation to the absorbed energy) as a function of peak laser power for gold foil target. The other laser beam parameters are the same as described above. The conversion efficiency of laser or ion beam to X-rays is of great significance for the indirect drive ICF schemes and its accurate estimation is of great importance. In this figure, the solid curves are the results from the present non-LTE model described in this paper. For the purpose of comparison we have also shown our LTE results in this figure (dotted lines). From this figure we observe that for both the LTE and non-LTE cases, the one group approximation overpredicts the conversion efficiency. We further observe that for all the laser intensity, the LTE conversion efficiency are more than the non-LTE estimates. The lower X-ray conversion efficiency in non-LTE conditions was also observed by Bodner [43] in his one-dimensional calculations. Another observation here is that in the case of multigroup non-LTE case (lowest curve in figure 14) the conversion efficiency reaches a maximum value for the laser intensity of 5.0×10^{13} W/cm^2 and then

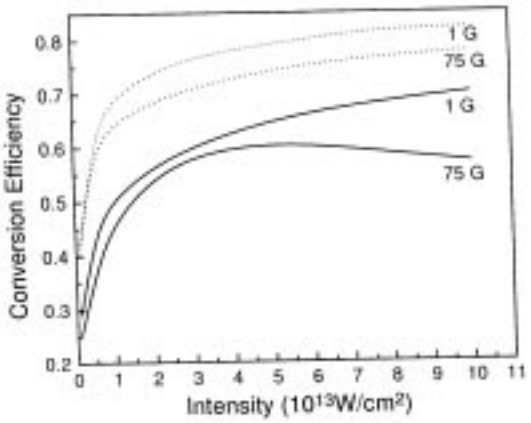

Figure 14. Computed conversion efficiencies of laser light as function of peak laser intensity for a 200 ps Gaussian beam for gold. Solid and dashed curves represent the results for non-LTE and LTE simulations. The curves marked 1 G and 75 G respectively denote the 1 and 75 frequency groups used in the radiation transport.

it decreases with the increasing laser power. This effect may not be a manifestation of numerical uncertainties as similar trend was also observed by Mead *et al* [44] where they have shown experimentally that there do exists a maximum in the conversion efficiency vs. laser power curve.

5. Conclusions

In this paper we have presented a non-local thermodynamic equilibrium model to calculate the frequency dependent absorption and emission coefficients for a mixture consisting of any number of elements. The steady state rate equations are solved to get the fraction density of various ions starting from neutral to fully ionized for each element in the mixture. The di-electronic recombination coefficient is included in the rate equations. The energy levels for the various ions present in the mixture are computed using the screened hydrogenic atom model including the ℓ splitting of the levels. It is seen that at high temperatures, the Thomas–Fermi and Saha model overestimate the ionization as compared to non-LTE model for gold. Non-LTE effects play a crucial role in the prediction of emitted spectrum of X-rays from the laser-driven thin gold foil. A comparison of LTE and non-LTE estimates of radiation-driven shock penetration depth with the experimental results show that non-LTE coefficients are necessary to explain the observed results. Studies on the effects of one group grey approximation and multi-group radiation transport on the hydrodynamic parameters of laser-driven aluminium and gold foils have shown that the radiation transport enhances the mass ablation rate. This in turn leads to higher ablation pressures as compared to the case when radiation transport is ignored. The conversion efficiency of laser light into X-rays shows that the one group approximation overpredicts the conversion efficiency. It is further seen that non-LTE effects play an important role in its prediction.

Acknowledgements

The authors are thankful to Dr. S K Sikka for many useful discussions and for his keen interest in this work.

References

[1] J D Lindl, *Inertial confinement fusion: The quest for ignition and energy gain using indirect drive* (Springer, New York, 1998)
[2] K Nishihara, M Murakami, H Azechi, T Jitsuni, T Kanabe, M Katayama, N Miyanaga, M Nakai, M Nakatsuka, K Tsubakimoto and S Nakai, *Phys. Plasmas* **1**, 1653 (1994)
[3] V F Ermolovich, G N Remizob, Yu A Romanov, N A Ryabikina, R M Shagaliev, L L Vakhlamova, V V Vatulin, O A Vinokurov, K H Kang, J A Maruhn and R Bock, *Laser and Particle Beams* **16**, 525 (1998)
[4] D Colombant, M Klapisch and A Bar Shalom, *Phys. Rev. Lett.* **57**, 3411 (1998)
T J Orzechowski, M D Rosen, H Kornblum, J L Porter, L J Suter, A R Thiessen and R J Wallace, *Phys. Rev. Lett.* **77**, 3545 (1996)
P Wang, J J MacFarlane and T J Orzechowski, *Rev. Sci. Instrum.* **68**, 1107 (1997)
H Nishimura, T Endo, H Shiraga, Y Kato and S Nakai, *Appl. Phys. Lett.* **62**, 1344 (1993)
[5] R M More, *J. Quant. Spectrosc. Radiat. Transfer* **27**, 345 (1982)
[6] G D Tsakiris and K Eidmann, *J. Quant. Spectrosc. Radiat. Transfer* **38**, 353 (1987)
[7] H Takabe, T Nishikawa and K Mima, *Statistical approach for calculating opacities of partially ionized high Z plasmas*, NIFS Research Report ISSN 0915-6348 (1991)
[8] A Rickert and J Meyer-ter-Vehn, *Laser and Particle Beams* **8**, 715 (1990)
[9] K Eidmann, Emission and absorption of radiation in laser-produced plasmas, in *Course and Workshop of the International School of Plasma Physics* edited by A Caruso and E Sinodoni, Bologna (1989)
[10] K G Whitney, J Davis and J P Apruzese, *Phys. Rev.* **A22**, 2196 (1989)
[11] S Kiyokawa, T Yabe and T Mochizukj, *Jpn. J. Appl. Phys.* **22**, L772 (1983)
[12] M Klapisch, A Bar-Shalom, J Oreg and D Colombant, *Phys. Plasmas* **5**, 1919 (1998)
[13] S E Bodner, D G Colombant, J H Gardner, R H Lehmberg, S P Obenchain, L Phillips, A J Schmitt and J D Sethian, *Phys. Plasmas* **5**, 1901 (1998)
[14] J J Honrubia, R Dezulian, D Batani, S Bossi, M Koenig, A Benuzzi and N Grandjouan, *Laser and Particle Beams* **16**, 13 (1998)
[15] R Marchand, C E Capjack and Y T Lee, *Phys. Fluids* **31**, 949 (1998)
[16] G C Pomraning, *The equations of radiation hydrodynamics* (Pergamon Press, Oxford, 1973)
[17] R Ramis, R Schmaiz and J Meyer-ter-Vehn, *Comput. Phys. Commun.* **49**, 475 (1988)
G B Zimmerman and W L Kruer, *Comments Plasma Phys. Controlled Fusion* **2**, 51 (1975)
[18] T Nishikawa, H Takabe and K Mima, *L-splitting effect and line profile modeling for average atom model*, NIFS Research Report ISSN 0915-6348 (1991)
[19] R L Kauffman, L J Suter, C B Darrow, J D Kilkenny, H N Kornblum, D S Montgomery, D W Phillion, M D Rosen, A R Theissen, R J Wallace and F Ze, *Phys. Rev. Lett.* **73**, 2320 (1994)
[20] C F Fischer, T Brage and P Joenleson, *Computational atomic structure* (IPP, Bristol, 1997)
[21] F Perrot, *Phys. Scr.* **39**, 332 (1989)
[22] G Faussurier, C Blancard and A Decoster, *J. Quant. Spectrosc. Radiat. Transfer* **58**, 233 (1997)
[23] T A Carlson, C W Nestor Jr., N Wassermann and J D McDowell, *Atomic Data and Nuclear Data Tables* **2**, 63 (1970)

[24] D Colombant and G Tonon, *J. Appl. Phys.* **44**, 3524 (1973)
[25] Ya B Zel'Dovich and Yu P Raizer, *Physics of shock waves and high temperature hydrodynamics phenomena* (Academic Press, New York, 1966)
[26] D E Post, R V Jensen, C B Tarter, W H Grasberger and W A Lokke, *Atomic Data and Nuclear Data Tables* **20**, 398 (1977)
[27] A Burgess, *Astrophys. J.* **141**, 1588 (1965)
[28] J J MacFarlane, *Comput. Phys. Commun.* **56**, 259 (1989)
[29] R M More, *Adv. Atom. Molec. Phys.* **21**, 305 (1985)
[30] D Mihalas and B W Mihalas, *Foundations of radiation hydrodynamics* (Oxford University Press, Oxford, 1984)
[31] I I Sobelman, *Atomic spectra and radiative transitions* (Springer-Verlag, Berlin, 1979)
[32] B H Armstrong and R W Nicholls, *Emission, absorption and transfer of radiation in heated atmosphere* (Pergamon Press, Oxford, 1972)
[33] A M Naqvi, *J. Quant. Spectrosc. Radiat. Transfer* **4**, 597 (1964)
[34] S J Rose, *J. Phys. B: At. Mol. Opt. Phys.* **25**, 1667 (1992)
[35] N K Gupta and B K Godwal, *Laser and Particle Beams* **19**, 259 (2001)
[36] R D Richtmyer and K W Morton, *Difference methods for initial value problem* (John Wiley, New York, 1967)
[37] L Spitzer, *Physics of fully ionized gases* (Wiley, New York, 1956)
S I Braginskii, in *Reviews of plasma physics* edited by M A Leontovich (Consultant Bureau, New York, 1965) vol. I
[38] N K Gupta and V Kumar, *Laser and Particle Beams* **13**, 389 (1995)
[39] P D Goldstone, S R Goldman, W C Mead, J A Cobble, G Stradling, R H Day, A Hauer, M C Richardson, R S Morjoribanks, R L Keck, F J Marshall, W Seka, O Barnouin, B Yaakobi and S A Letzring, *Phys. Rev. Lett.* **59**, 56 (1987)
[40] K S Holian (ed.), *T-4 handbook of materials properties data base*, Vol. 1c: Equation of State, La-10160, UC-34 (1984)
[41] V Yu Bychenkov and V T Tikhonchuk, in *Nuclear fusion by inertial confinement: A comprehensive treatise* edited by G Velarde, V Ronen and J M Martinz-val (C. R. C. Press, 1992) Ch. 3, p. 73
[42] K Eidmann, R F Schamatz and R Sigel, *Phys. Fluids* **B2**, 208 (1990)
[43] S E Bodner, *Comments Plasma Phys. Controlled Fusion* **16**, 351 (1995)
[44] W C Mead, E K Stover, R L Kauffman, H N Kornblum and B F Lasinski, *Phys. Rev.* **A38**, 5275 (1988)